AGU PUBLICATIONS

JGR

Journal of Geophysical Research: Solid Earth

RESEARCH ARTICLE
10.1002/2016JB012858

Key Points:
- Complete study of El Mayor-Cucapah coseismic displacement, fault geometry, and slip distribution
- We investigate consistency of inferred slip on the faults by varying Earth structure and choice of geodetic constraints
- Apparent shallow slip deficits can be related to fault geometry discretization, smoothing, and geodetic constraints

Supporting Information:
- Supporting Information S1
- Data Set S1
- Data Set S2
- Data Set S3

Correspondence to:
M.-H. Huang,
Mong-Han.Huang@jpl.nasa.gov

Citation:
Huang, M.-H., E. J. Fielding, H. Dickinson, J. Sun, J. A. Gonzalez-Ortega, A. M. Freed, and R. Bürgmann (2016), Fault geometry inversion and slip distribution of the 2010 M_w 7.2 El Mayor-Cucapah earthquake from geodetic data, *J. Geophys. Res. Solid Earth*, *121*, doi:10.1002/2016JB012858.

Received 2 FEB 2016
Accepted 11 NOV 2016
Accepted article online 15 NOV 2016

Fault geometry inversion and slip distribution of the 2010 M_w 7.2 El Mayor-Cucapah earthquake from geodetic data

Mong-Han Huang[1], Eric J. Fielding[1], Haylee Dickinson[2], Jianbao Sun[3], J. Alejandro Gonzalez-Ortega[4], Andrew M. Freed[2], and Roland Bürgmann[5,6]

[1]Jet Propulsion Laboratory, California Institute of Technology, Pasadena, California, USA, [2]Department of Earth, Atmospheric, and Planetary Sciences, Purdue University, West Lafayette, Indiana, USA, [3]State Key Laboratory of Earthquake Dynamics, Institute of Geology, China Earthquake Administration, Beijing, China, [4]Institute of Geophysics and Planetary Physics, Scripps Institution of Oceanography, University of California, San Diego, La Jolla, California, USA, [5]Department of Earth and Planetary Science, University of California, Berkeley, California, USA, [6]Berkeley Seismological Laboratory, University of California, Berkeley, California, USA

Abstract The 4 April 2010 M_w 7.2 El Mayor-Cucapah (EMC) earthquake in Baja, California, and Sonora, Mexico, had primarily right-lateral strike-slip motion and a minor normal-slip component. The surface rupture extended about 120 km in a NW-SE direction, west of the Cerro Prieto fault. Here we use geodetic measurements including near- to far-field GPS, interferometric synthetic aperture radar (InSAR), and subpixel offset measurements of radar and optical images to characterize the fault slip during the EMC event. We use dislocation inversion methods and determine an optimal nine-segment fault geometry, as well as a subfault slip distribution from the geodetic measurements. With systematic perturbation of the fault dip angles, randomly removing one geodetic data constraint, or different data combinations, we are able to explore the robustness of the inferred slip distribution along fault strike and depth. The model fitting residuals imply contributions of early postseismic deformation to the InSAR measurements as well as lateral heterogeneity in the crustal elastic structure between the Peninsular Ranges and the Salton Trough. We also find that with incorporation of near-field geodetic data and finer fault patch size, the shallow slip deficit is reduced in the EMC event by reductions in the level of smoothing. These results show that the outcomes of coseismic inversions can vary greatly depending on model parameterization and methodology.

1. Introduction

The 4 April 2010 M_w 7.2 El Mayor-Cucapah (EMC) earthquake in Baja, California, and Sonora, Mexico, ruptured ~60 km of the Laguna Salada-Cañada David fault system north of the epicenter with primarily right-lateral strike-slip motion. South of the epicenter, another ~60 km of surface rupture occurred across the Colorado River delta, which had no mapped active faults before this event [*Fletcher et al*., 2014]. The trace of the surface rupture has been well resolved by differential lidar [*Oskin et al*., 2012; *Gold et al*., 2013], subpixel correlation analysis of optical and radar data [*Wei et al*., 2011], and field observations [*Fletcher et al*., 2014]. Although this event shows dominant strike-slip motion (up to 5 m), vertical displacement (up to 2 m) is observed along the entire length of the rupture and reflects a significant component of normal slip [*Oskin et al*., 2012; *Fletcher et al*., 2014]. The earthquake ruptured a complex set of faults that lie to the west of the Cerro Prieto fault and are part of a dextral-normal fault system in the southern Salton Trough with multiple sets of active faults, similar to Southern California (Figure 1). *Wei et al*. [2011] combined seismic and geodetic data sets to investigate slip distribution on a four-segment fault geometry. They found that the high nondouble-couple component of the seismic moment tensor (~25% of the total moment) occurred because the earthquake initiated from a secondary north striking and east dipping normal fault and subsequently ruptured bilaterally northwestward along a 75° east dipping fault and southeastward along a 60° west dipping fault. More than 9500 aftershocks occurred within 2 months of the EMC main shock. In the northern ruptures, aftershock relocations reveal a complex en echelon and conjugate fault system toward the northwest of the fault surface rupture [*Kroll et al*., 2013]. The largest M_w 5.7 aftershock occurred on 14 June 2010 near Ocotillo (Figure 1a), northwest of the north end of the surface rupture.

The crustal thickness across the region varies from 10 km in the Pacific Plate to about 35 km in the Peninsular Ranges, ~22 km in the Salton Trough, and then ~25 km toward Southern Colorado River Desert in Arizona [*Tape et al*., 2009, 2012; *Shaw et al*., 2015]. In the Salton Trough near the EMC event, there is a distinct region

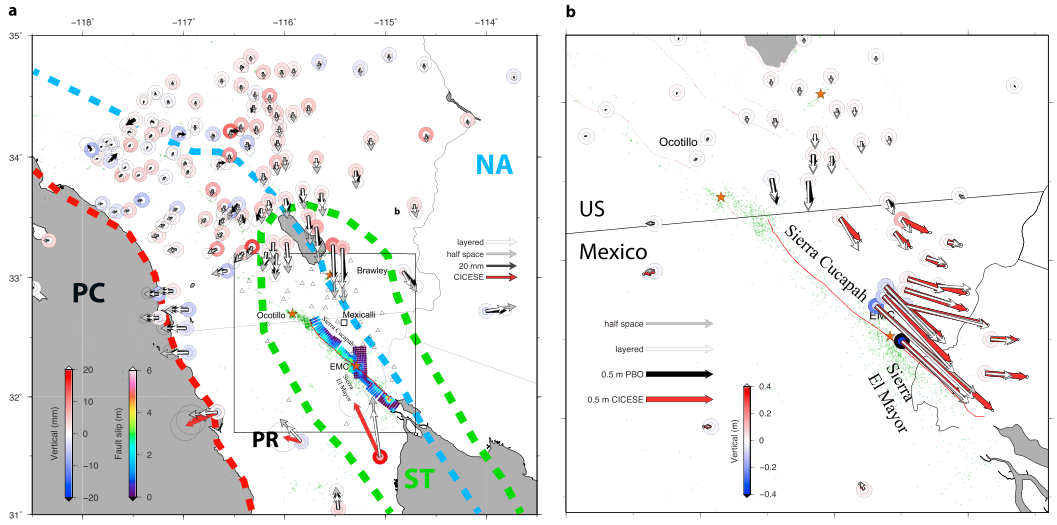

Figure 1. GPS coseismic displacements (black and red arrows) and model fitting (white and grey arrows). (a) GPS coseismic displacement (data, homogeneous, and layered model predictions). The thick dashed lines denote the different tectonic boundaries with the green outlining the Salton Trough and the blue line illustrating the different tectonic regions in the study area. The red curved line is the earthquake surface rupture, and the red stars show the EMC main shock, the largest aftershock, and the Brawley earthquake swarms. The white triangles are the locations of GPS stations shown in Figure 1b. (b) Detail of GPS coseismic displacement nearby the Salton Trough. PC–Pacific Plate; PR–Peninsular Range; ST–Salton Trough; NA–North America. Note the different scale for displacements in Figures 1a and 1b.

of high crustal heat flow [*Blackwell and Richards*, 2004], as well as shallower Moho and lithosphere-asthenosphere boundary depths [*Lekic et al*., 2011; *Shaw et al*., 2015], which implies varied crustal rheology across different geologic units.

In this study, we process coseismic synthetic aperture radar (SAR) interferograms with ascending and descending orbits and subpixel offset measurements on SAR and optical images to reveal coseismic displacements. We develop a nine-segment fault geometry with shallower parts constrained by mapped surface ruptures and fault dipping angles optimized from the GPS, interferometric synthetic aperture radar (InSAR), and subpixel offset measurements. The slip distribution on each fault segment is determined with geodetic inversions in either a homogeneous or a layered Earth structure. We use the model fitting residuals to find evidence of crustal-scale lateral heterogeneity, and we also investigate the phenomenon of shallow slip deficit (where coseismic slip decreases as the surface is approached) with extensive geodetic data. Our goal is to rigorously reveal detailed fault geometry as well as slip localization during the EMC event and to objectively investigate model sensitivity based on different data constraints.

2. Geodetic Data

The EarthScope project Plate Boundary Observatory (PBO) began installation and maintenance of 891 continuous GPS (CGPS) sites in the western U.S. in 2003 [*Spinler et al*., 2015]. We obtain 132 EMC coseismic GPS measurements through the University NAVSTAR Consortium (UNAVCO) Data Center (ftp://data-out.unavco.org/pub/products/sinex/; Figure 1). In addition to the PBO network in the U.S., we also processed the GPS campaign data from northern Baja California with the GAMIT/GLOBK processing package, version 10.4 [*Herring et al*., 2008]. In the first step the package uses double-difference phase data between GPS satellites and stations to solve for station coordinates, atmospheric zenith delays, and integer ambiguities for a full UTC day in a loosely constrained solution covariance matrix. Next, GLOBK software is used to estimate velocities by combining the loosely constrained solution with the International Global Navigation Satellite System solution from Scripps Orbit and Permanent Array Center for all surveyed sites in the International Terrestrial Reference Frame 2008 reference frame.

The GPS data used to calculate the interseismic crustal velocity for northern Baja California are archived at the Southern California Earthquake Center, UNAVCO, and Centro de Investigación Científica y de Educación

Table 1. InSAR Data Used in This Study

ALOS PALSAR

Track	Master (dd/mm/yyyy)	Slave (dd/mm/yyyy)	Geometry Inversion	Slip Inversion
A210	31/03/2010	16/05/2010		X
A211	15/01/2010	17/04/2010	X	X
A212	17/12/2009	04/05/2010	X	X
D533	30/11/2009	17/04/2010		X

Envisat ASAR

Track	Master (dd/mm/yyyy)	Slave (dd/mm/yyyy)	Geometry Inversion	Slip Inversion
A077	28/03/2010	02/05/2010	X	X
A306	09/03/2010	13/04/2010	X	X
D084	12/03/2010	16/04/2010	X	X
D313	28/03/2010	02/05/2010		X
D356	09/03/2010	13/04/2010	X	X

Superior de Ensenada (CICESE) database servers, whereas the GPS campaign survey for measuring the surface displacements after the El Mayor-Cucapah earthquake was conducted by teams from CICESE, University of California, San Diego, and University of California, Riverside. Interseismic position corrections were made using our preseismic velocity field for northern Baja California extrapolated over time after the earthquake. This extrapolated position was then subtracted from the new position to obtain the coseismic displacements.

We use five tracks of *Environmental Satellite* (Envisat) advanced synthetic aperture radar (ASAR; 5.6 cm wavelength) acquisitions and four tracks of *Advanced Land Observing Satellite* (ALOS) Phased Array type L-band Synthetic Aperture Radar (PALSAR; 23.5 cm wavelength) acquisitions to generate coseismic interferograms. The Envisat satellite was operated by the European Space Agency and the ALOS satellite by the Japan Aerospace Exploration Agency. We use ROI_PAC version 3.0.1 [*Rosen et al*., 2004] to generate interferograms and the 1 arc sec resolution Shuttle Radar Topography Mission digital elevation model to correct the phases due to topography. *Snaphu* 1.4.2 [*Chen and Zebker*, 2002] is used for the phase unwrapping. Nine ASAR and PALSAR interferograms in both ascending and descending tracks (Table 1) capture the coseismic displacements (Figures 2a, 2b, and S1 in the supporting information). Note that some acquisitions were acquired as late as 42 days after the main shock and therefore contain some postseismic displacement.

We apply the subpixel correlation or pixel offset tracking method [e.g., *Michel et al*., 1999] on optical and SAR images to measure the large coseismic displacements [*Wei et al*., 2011]. This method calculates offsets between two amplitude images along satellite cross-track (called range for SAR) and along-track (called azimuth for SAR) directions. The *Satellite Pour l'Observation de la Terre 5* (SPOT-5) optical images were processed with the COSI-Corr package [*Leprince et al*., 2007] and are the same as those used by *Wei et al*. [2011]. The Envisat and ALOS SAR image offsets were processed using the spatial correlation module (*ampcor*) included in the ROI_PAC package. The SAR range offsets were corrected for the topographic displacements and orbital baseline using the ROI_PAC *IntSim* and *diffnsim* programs, but the azimuth offsets were empirically corrected for orbits by trend removal. For SPOT-5 images both directions are horizontal, so we can convert them into north-south and east-west components. For SAR amplitude images, the range direction is the same as the line of sight in InSAR and has both horizontal and vertical components. The SAR azimuth offsets are horizontal in the satellite motion direction. We use 64 by 64 pixel matching windows sliding at every 16 pixels of the full resolution images for both the offset calculations. The resolution of this method is about 1/5 to 1/20 of the pixel size, so the theoretical offset precision is 0.13 m for SPOT-5 (2.5 m pixels) and about 0.3 m for ALOS and Envisat (between 4 and 8 m pixel sizes depending on mode). Figures 2c, 2d, and S2 show the seven subpixel offset data sets used in the coseismic slip modeling.

We resample both InSAR and subpixel offset results using a fault slip resolution-optimized quadtree partitioning algorithm [*Lohman and Simons*, 2005]. This method gives denser sampling in areas closer to the fault to preserve detail of displacement in the near field and reduces samples in areas where the displacements are not providing as much resolution on the fault slip. The assumed fault trace can be relatively simple. We used two large rectangular faults that approximately match the faults used in *Wei et al*. [2011],

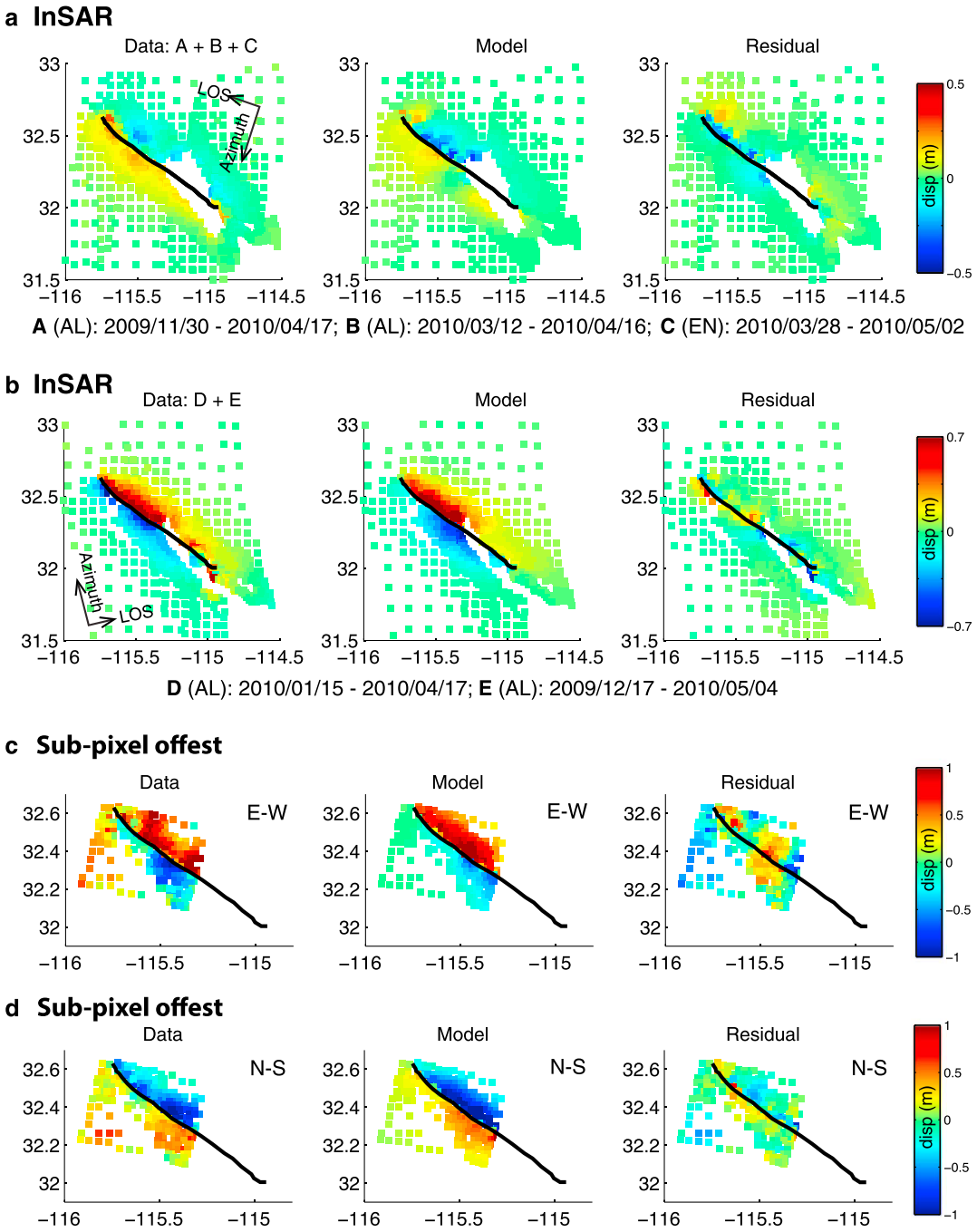

Figure 2. Selected InSAR and subpixel offset results. (a and b) The InSAR data, model prediction, and model residual for descending (Figure 2a) and ascending (Figure 2b) orbits. Note that the InSAR descending/ascending data are a stack of some interferograms, where the pairs are listed below each figure. (c and d) The subpixel offset results of a SPOT image pair, where Figure 2c shows east-west and Figure 2d shows north-south components. Each model result shown is in a layered Earth structure. See Figure S1 for a complete set of InSAR data and modeling fitting and Figure S2 for a complete set of subpixel offset results of SAR images.

northern fault dipping east and southern fault dipping west, as the starting model faults for the fault resolution-based resampling. The surface traces of the faults are well known, and that is the most important parameter of the faults used for sampling. After this subsampling, there are 4447 pixels left from 9 interferograms and 1341 pixels from 4 subpixel offset images (Figures 2, S1, and S2). For InSAR, some interferograms contain long-wavelength tilt due to orbital error or large-scale atmospheric variations that

Table 2. Subpixel Offset Data Used in This Study

SPOT5 (Range and Azimuth)

Master (dd/mm/yyyy)	Slave (dd/mm/yyyy)	Geometry Inversion	Slip Inversion
26/05/2009	08/04/2010	X	X

SAR

Track	Master (dd/mm/yyyy)	Slave (dd/mm/yyyy)	Satellite	Geometry inversion	Slip inversion
A306 (range and azimuth)	09/03/2010	13/04/2010	Envisat		X
A211 (azimuth)	15/01/2010	17/04/2010	ALOS	X	X
A212 (azimuth)	17/12/2009	04/05/2010	ALOS	X	X
D313 (range and azimuth)	28/03/2010	02/05/2010	Envisat		X

is not related to far-field coseismic displacement (Figure S5). To reduce this perturbation we calculate the tilt by fitting a linear plane to each interferogram using least squares as part of the slip inversion and then remove the plane from affected interferograms. The interferograms used in this study are wider or longer than the area of coseismic displacement, so removing the tilt does not affect InSAR coseismic measurements.

3. Coseismic Fault Geometry

The fault geometry proposed by *Wei et al*. [2011] is composed of four fault planes, including two east dipping planes north of the epicenter, one west dipping fault plane south of the epicenter, and one N-S striking normal fault near the epicenter. In our approach, we first use the surface rupture data [*Fletcher et al*., 2014] to determine fault length, segments, and fault trace. We use geodetic data (GPS, InSAR, and subpixel offset measurements) to determine fault dip angles and then the slip distribution.

Our InSAR and subpixel offset data also show some coseismic displacements south of the mapped surface rupture (Figures 2 and S2), so we extend the fault geometry ~20 km further south from the southern end. Initially, we fix the strike of each fault segment and the horizontal location of the top edges, since there are clear surface ruptures for most of the fault zone [*Fletcher et al*., 2014]. We then increase the number of fault segments in order to better capture the mapped main EMC surface rupture. The final fault geometry model has five northern segments and three southern segments along the fault surface ruptures, and the fault dip angles are between 56° and 69° for the five northern segments and between 50° and 65° for the three southern segments. To constrain dip angle of each fault segment, we hold the top edge location fixed and optimize the solution for dip and slip distribution on each of these eight fault segments simultaneously.

We choose 15 data sets (the GPS displacements, 9 interferograms, and 5 subpixel offset data sets; see Tables 1 and 2) for the geometry inversion. We use formal inversion methods based on the maximum a posteriori probability method proposed by *Sun et al*. [2013], which belongs to the optimization class of Monte Carlo methods. The fault dips and the slip distribution of the eight segments, along with the weight of each data set and the Laplacian smoothing factor, are all resolved in one process using the Adaptive Simulated Annealing global optimization algorithm [*Ingber*, 1993] to maximize the posteriori probability density functions. To reduce computational cost, the Okada solution [*Okada*, 1992] assuming a homogenous half-space Earth structure is used to calculate the surface deformation in the geometry optimization. We later vary the dip angles of the five east dipping faults and the three west dipping faults by up to 5° in the layered Earth structure in order to test the consistency of slip distribution with slightly different fault dip angles. The data sets with larger noise, such as the strong ionospheric signals of L-band SAR data, the large noise on the N-S component of the SPOT subpixel data, and the heavy atmospheric noise of C-band SAR data, are excluded from the geometry inversion to avoid possible bias of the solution.

After we determined the optimal geometry as mentioned above, we added the N-S normal fault as a ninth fault at the epicenter proposed by *Wei et al*. [2011], which can explain the first 15 s of the teleseismic waveforms. We optimized the strike and dip of this normal fault while holding the other eight faults fixed to fit the geodetic data. With the final nine fault geometry, we perform analysis of the effects of changing the Earth elastic structure and of choosing different input data sets on the slip inversions holding the geometry of the nine faults fixed. Each fault segment is discretized into 2 km × 2 km subfaults (Table S1). To calculate

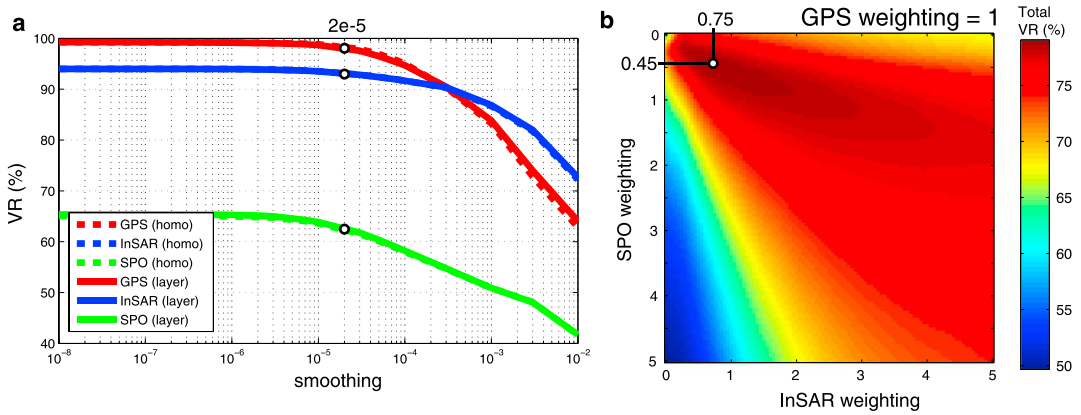

Figure 3. Variance reduction (VR) as a function of (a) smoothing and (b) GPS weighting. In Figure 3a, the dashed lines are the inversions considering a homogeneous Earth structure and the solid lines show the inversions considering a layered structure. The inferred smoothing parameter is 2×10^{-5} for this study. SPO denotes subpixel offset. In Figure 3b GPS weighting is fixed as 1 and either InSAR of subpixel offsets (SPO) are varied between 0 and 5. The preferred weighting between GPS, InSAR, and SPO is 1, 0.75, and 0.45.

coseismic slip and rake of each subfault, we use dislocation models in a layered elastic structure. We compute Green's functions in a 100 km thick layered medium as used by *Wei et al*. [2011] (Table S2) by using the EDGRN/EDCMP code [*Wang et al*., 2003]. We also calculate slip distribution in a homogeneous elastic structure for comparison. We use a nonnegative least squares routine to calculate the amount of slip and rake of each subfault. For each subfault, we allow rake to vary between 135° and 225°, representing a right-lateral strike-slip dominated motion with some updown or downdip component. We apply a smoothing parameter between subfaults following *Huang et al*. [2013] to avoid model overfitting or underfitting, and we do not assign damping of slip at the edges of fault segments. This method depicts the smoothing by plotting the smoothing value versus variance reduction (VR) curve and then chooses the smoothing value when further decreasing smoothing does not significantly improve the fit variance reduction ($\mathrm{VR} = \left[1 - \frac{\sum_i (d_i - s_i)^2}{\sum_i d_i^2}\right] \times 100$, where d_i is the observed data and s_i is its prediction based on the model) (Figure 3a). For slip inversions we include more InSAR and subpixel offset data sets (Tables 1 and 2) in order to increase the number of geodetic constraints. For joint inversions, we determine the weighting between GPS, InSAR, and subpixel offset data sets. We weight InSAR and subpixel offset data sets equally and then vary the GPS weighting, while the InSAR and subpixel offset weighting are fixed. We compare the VR of each data set with different GPS weightings (Figure 3b) and determine the GPS weighting when the joint VR is the highest [*Huang et al*., 2013].

4. Model Results

We test GPS, InSAR, and subpixel offset inversions individually and jointly, all with the same fault geometry. For each set of constraints, we invert for slip based on a homogeneous or a layered Earth structure (Table S2). We first compare VR of inversions with different smoothing parameters (Figure 3a) and determine the amount of smoothing for a relatively smooth slip model while still maintaining high VR. To determine relative weighting between data in the joint inversions, we choose the same smoothing parameter and then compare VR of each data set while varying the GPS weighting (Figure 3b). Figures 1a and 1b show the GPS fitting based on a homogeneous or layered Earth structure, and Figures 2, S1, and S2 show the InSAR and subpixel offset fitting based on different data constraints. Table 3 summarizes the VR of each set of data constraints and Earth structure. In general, the inversions can best fit the GPS data ($\mathrm{VR} > 96\%$), followed by InSAR ($\mathrm{VR} > 87\%$), and subpixel offsets ($\mathrm{VR} > 51\%$).

For GPS fitting in joint inversion, the VRs of homogeneous and layered Earth structure are similar (Table 3), but the layered structure model fits far-field stations better (Figure 1a). On the other hand, the homogeneous Earth model can fit near-field stations slightly better (Figure 1b). The predicted slip distribution is similar along the five northern fault segments under the Sierra Cucapah (Figure 4b), but the layered structure model has significantly higher slip in the three southern fault segments located far from the GPS stations.

Table 3. Individual and Combined Geodetic Inversions

I. Homogeneous Earth Structure

	M_o (N m)	M_w	VR (%) (A)	VR (%) (B)	VR (%) (C)
GPS (A)	8.9×10^{19}	7.26	98.7	NA	NA
InSAR (B)	8.1×10^{19}	7.23	NA	93.1	NA
Pixel offset (C)	9.2×10^{19}	7.27	NA	NA	61.8
(A) + (B)	8.2×10^{19}	7.24	95.0	93.0	NA
(A) + (C)	8.8×10^{19}	7.26	93.6	NA	61.4
(B) + (C)	8.3×10^{19}	7.24	NA	88.9	56.8
(A) + (B) + (C)	8.2×10^{19}	7.24	95.2	89.0	56.6

II. Layered Earth Structure

	M_o (N m)	M_w	VR (%) (A)	VR (%) (B)	VR (%) (C)
GPS (A)	10.9×10^{19}	7.32	97.87	NA	NA
InSAR (B)	9.5×10^{19}	7.29	NA	93.1	NA
Pixel offset (C)	10.5×10^{19}	7.31	NA	NA	65.56
(A) + (B)	8.2×10^{19}	7.21	96.2	92.1	NA
(A) + (C)	8.1×10^{19}	7.20	96.4	NA	61.3
(B) + (C)	8.9×10^{19}	7.23	NA	87.3	58.5
(A) + (B) + (C)	9.6×10^{19}	7.28	96.6	87.9	51.8

The InSAR slip model shows slip at shallower depth in segments 1–6 and at deeper depth in segments 7 and 8 (Figure 4b). The VRs of InSAR fitting are also similar between the two structure models (Table 3) but lower than those found in the GPS inversion. This is possibly due to higher sampling density and uncertainty (~1 cm) in the InSAR data, as well as more complex near-field displacements associated with unmodeled secondary fault ruptures included in the InSAR. In this study we do not include secondary faults at shallower depths or inelastic deformation in the near field, and therefore, higher data misfit is found in the near field (Figures 2a, 2b, S1, and S2). In addition, the coseismic interferograms contain up to 42 days of postseismic deformation that cannot be separated by InSAR-only inversions.

The VRs of subpixel offset data are significantly lower than GPS or InSAR for models from either structure models. This data set contains more very near-field observations, and the higher uncertainty (~0.25 m) of this data set also contributes to worse fitting. Some of the ALOS L-band SAR offsets are affected by ionospheric variations that add larger errors to the measurements. Figures 2c, 2d, and S2 show the higher model misfit in both near and far fields of the SPOT, Envisat, and ALOS image offset data sets. The model inverted from the subpixel offsets alone predicts higher slip in fault segments 3, 4, 6, and 8 but lower slip in segments 1 and 2 (Figure 4a). The peak slip amplitude is ~4.5 m in segment 4.

For the joint inversions, the VR of the joint inversion is lower than that in individual inversions, as expected, because it is a combination of different data constraints (Table 3 and Figure 3b). The inferred slip is a mixture of features found in individual inversions, including shallower (0–10 km) slip in fault segments 1–5 and a bulls-eye shape of slip in segment 8 (Figure 4a). The slip pattern is similar between the homogeneous and layered structure models, but there is substantially more deep slip in segment 6 in the layered structure model.

5. Discussion

5.1. Slip Consistency in Different Data Sets and Inversions

Our synthetic checkerboard tests (Text S1 in the supporting information) demonstrate how reliable the inverted slip is, given the geodetic data constraints and uncertainties. Although GPS measurements have the lowest data uncertainty and provide three-dimensional measurements, the GPS network is very heterogeneous as there are more than 100 PBO CGPS stations north of the U.S.-Mexico boundary (Figure 1). This heterogeneous network density limits the ability of resolving distinct slip patches especially in the southern fault segments (Figures 4 and S4).

For the inversions with InSAR constraints, there are more than 4000 selected InSAR pixels from 9 interferograms (Figures 2a, 2b, and S1) that uniformly cover the coseismic surface ruptures, so the resolution of each fault segment is about the same (Figures 5a and S5). However, long-wavelength perturbations in the

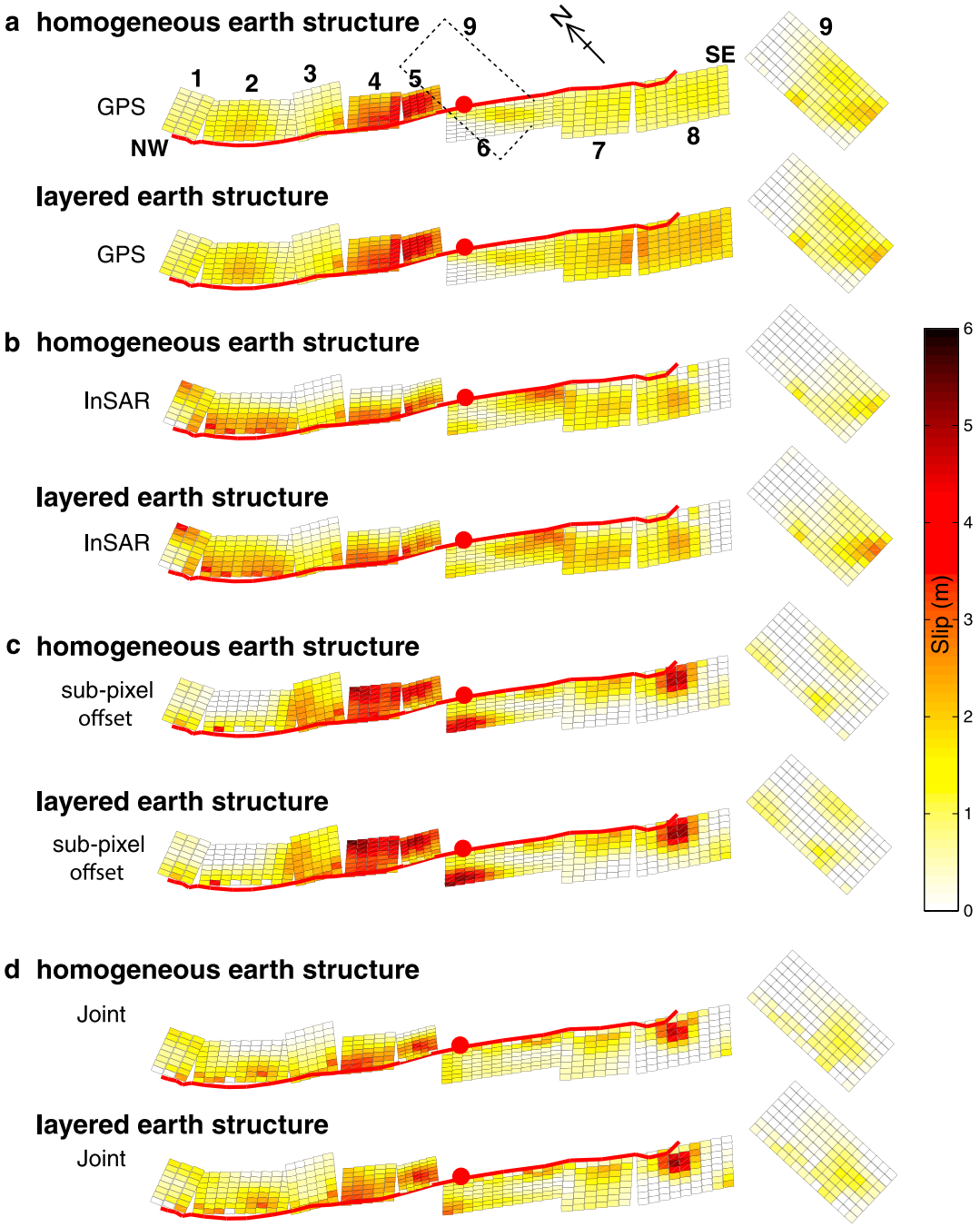

Figure 4. Comparison of (a) GPS, (b) InSAR, (c) subpixel offset, and (d) joint inversion with using homogeneous or layered Earth structure. The red circle represents the earthquake epicenter, and the red line demonstrates the surface rupture.

interferograms due to orbital error, atmospheric delay, and local topographic relief [*Bürgmann et al.*, 2000] may significantly contaminate the coseismic signals. As a result, in the far field where InSAR noise is higher than the observed displacement or in the mountain ranges (e.g., Sierra El Mayor) where InSAR signals contain higher topography-correlated phase, InSAR may not be able to resolve coseismic displacement in those regions (Figure S5).

For the subpixel offset inversions, there are more near-field data samplings with >1 m of displacement that are not revealed by InSAR. However, the highest precision of this technique is about 1/20 of the image pixel size [*Wei et al.*, 2011], which is ~0.15 m for SPOT images and ~0.3 m for ALOS or Envisat SAR images. In

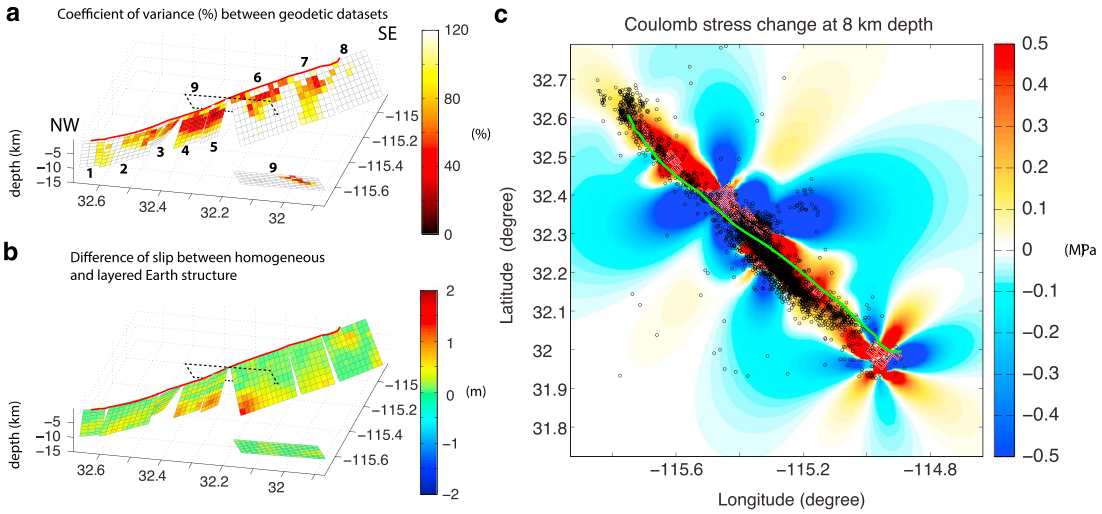

Figure 5. Slip model consistency and the inferred slip distribution. (a) Standard deviation of slip between different combinations of geodetic data. (b) Difference (layered model-homogeneous model) of inversions with homogeneous and layered structures. (c) Coseismic Coulomb stress change at 8 km depth. The input slip model is based on the slip model of joint inversion. The red and blue colors represent the stress positive and negative stress changes, respectively. The black dots are the aftershocks of the first year (RESNOM; http://resnom.cicese.mx/), and the green line is the main EMC surface rupture.

addition, the ROI_PAC software does not completely compensate for the SAR geometry effects on the measured SAR offsets, and other errors affect the SPOT offsets so the long-wavelength offset signals are inaccurate. According to our InSAR result (Figures 2a and S1), only near-field coseismic displacements are above the subpixel offset precision and accuracy. As a result, the subpixel offset inversions only constrain shallow slip in the inversions (Figure 4).

Due to higher atmospheric noise (both turbulent and topographically correlated troposphere and ionosphere) in the InSAR and subpixel offset measurements, we include more InSAR and subpixel offset data to reduce model sensitivity to nonearthquake-related noise and to prevent data overfitting. The selected nine interferograms and five subpixel offsets cover the entire fault surface ruptures and far-field region, in ascending and descending tracks with different look angles. In other words, displacements at each subregion near-surface ruptures are observed in different look directions. Although only selecting interferograms that have best coverage and lower noise level is also feasible, the inferred slip distribution may have a higher chance of being biased due to overfitting certain details of the noise structure in one interferogram or pixel offset map.

In order to evaluate the consistency of slip distribution with different data constraints (Table 3), we calculate the coefficient of variance (CV; standard deviation divided by mean slip) of each subfault from all the individual and combined data set inversions. As shown in Figure 5a, there is higher slip consistency (i.e., lower CV) at segments 3–6, as well as at shallower depths in general. At segment 8, higher CV may reflect that the large slip found in subpixel offset inversions (which have a strong near-field signal) is not well imaged in GPS or InSAR inversions because there are fewer data samples in the near field. Similar to the checkerboard tests, the slip deviation test shows higher deviation at greater depth, implying that we have better resolution at shallower depths. We also perform a jackknife test by iteratively removing one InSAR or subpixel offset data set in each inversion and then calculating the mean slip distribution, standard deviation of slip, and the coefficient of variation (CV), which is shown in Figure S5. The CV results imply more consistent slip (dark color) in InSAR inversions, than in inversions of subpixel offsets, and also higher consistency in shallower slip than in deeper slip for both data sets.

We also calculate the difference in slip between homogeneous and layered Earth structures to highlight how the Earth structure could influence the inverted slip. This is because when shear modulus increases with depth, more deep slip is needed to achieve the same amount of surface displacements [*Hearn and Bürgmann*, 2005]. As shown in Figure 5b (homogeneous model subtracted from layered model), most of the slip difference is located at greater (10–15 km) depth. Similar to CV in the slip between data sets (Figure 5a), the highest slip difference is located at segment 6 with a peak slip difference of ~1.6 m (~60% at 12 km depth) solely due to the choice of homogeneous or layered Earth structure. For joint inversions,

varying the Earth structure from homogeneous to layered results in an M_w change from 7.24 to 7.28 (Table 3). In addition to slip discrepancy led by the choice of Earth models, *Du et al*. [1997], *Cattin et al*. [1999], and *Segall* [2010] documented bias in fault depth and difference in predicted surface displacement with using homogeneous or layered Earth structure. Similarly, we find bias in the amount of deep fault slip and inferred moment due to change of shear modulus at depth in the layered Earth structure, as shown in Figure 5b.

In order to test the possibility of slip distribution being biased due to slight change of optimized fault dip angle between a homogeneous or a layered Earth structure, we systematically vary fault dip angles by 0°, 3°, and 5° in both directions (i.e., 5 variations) on either west or east dipping faults (i.e., $5^2 = 25$ combinations) in the layered Earth structure. We do not attempt to vary the dip angle of individual fault segments due to more expensive computation (i.e., $5^9 = 1{,}953{,}125$ combinations). We invert for the slip distribution from the 25 combinations of dip angle variation and then calculate the coefficient of variance and standard deviation. Figure S6 shows the standard deviation and CV of slip on each subfault. We find that the standard variation is generally lower than 50 cm except the deepest slip at the NW corner of the fault segment 6. The CV is generally lower than 30% in all subfault patches, and the CVs of the patches that are higher than 60% are essentially at the locations with slip lower than 0.3 m. As a result, the slip distribution is relatively stable even when fault dip angles are varied by $\pm 5°$.

We have demonstrated that each fault segment has different spatial resolution at varying depths according to different data constraints within our inversions. In the joint inversion, we can separate multiple slip patches at shallower depth in segments 1 and 2. The peak slip of the northern segments is located between segments 3 and 4. In the southern segments, the slip is distributed at a greater depth in segment 6 and then migrates toward shallower depths to the south. The peak slip of the southern segments is ~4 m on segment 8, and we find a smaller slip patch (~2 m) at segment 7. Overall, the inferred slip model in this study is consistent with the joint seismic-geodetic or geodetic-only inversions proposed by *Wei et al*. [2011], but there is more deep slip (10–15 km) at segment 6 in this study (Figure 4), which is likely due to the subpixel offset data. In this study we include eight different subpixel offset results (Table 2), adding an additional four data sets to those used by *Wei et al*. [2011]. We consider all of the subpixel offset results in order to preserve features that may not be detected by other data sets, but we also admit that higher subpixel uncertainty could possibly contribute to this deep slip patch. The deep slip on segment 6 could also be due to slip on the north striking normal fault that we are not including in our fault geometry. The GPS and InSAR inversions have large slip on this segment, but the near-field pixel offsets indicate that it cannot be close to the surface here so the joint inversion puts it deeper on segment 6.

5.2. Comparison With Aftershocks

We calculate the Coulomb stress change based on our fault geometry and slip distribution using the Coulomb 3.3 software [*Toda et al*., 2011]. As shown in Figure 5c, when assuming a NW-SE strike-slip fault as the receiver fault, the areas with positive stress change (red color) is collocated with where the first-year aftershocks occurred (data from RESNOM; http://resnom.cicese.mx/). This implies that aftershocks occurred at the locations where faults are brought closer to failure. On the other hand, fewer aftershocks are observed near segment 5, which is in agreement with negative Coulomb stress change (i.e., faults are brought away from failure) in this area. We also find that aftershocks become more diffuse near segment 5 near the epicenter, perhaps indicating a transition from the east dipping fault geometry to a west dipping fault plane east of the Sierra El Mayor. Most of the inferred slip is shallower than the aftershock sequence except for the deepest slip at fault segment 6. However, as discussed in section 5.1, slip at this depth range is not well resolved.

Along the coseismic surface ruptures, the aftershock sequence from the standard catalog of RESNOM does not seem to extend south of the southern surface rupture (Figure 5c), where positive Coulomb stress change as well as more than 50 mm of postseismic displacement are observed [*Gonzalez-Ortega et al*., 2014]. In addition, there are not as many aftershocks in the southernmost segment as in the northmost segment, even though a 4 m slip is inferred here, which could be caused by the smaller number of seismic stations south of the Mexicali Valley due to the Gulf of California and limited access to the south.

5.3. Computed Moment

The main slip difference between homogeneous and layered Earth models is at the bottom of the fault geometry (Figure 6b) due to higher shear modulus with depth (Table S2). This higher shear modulus would

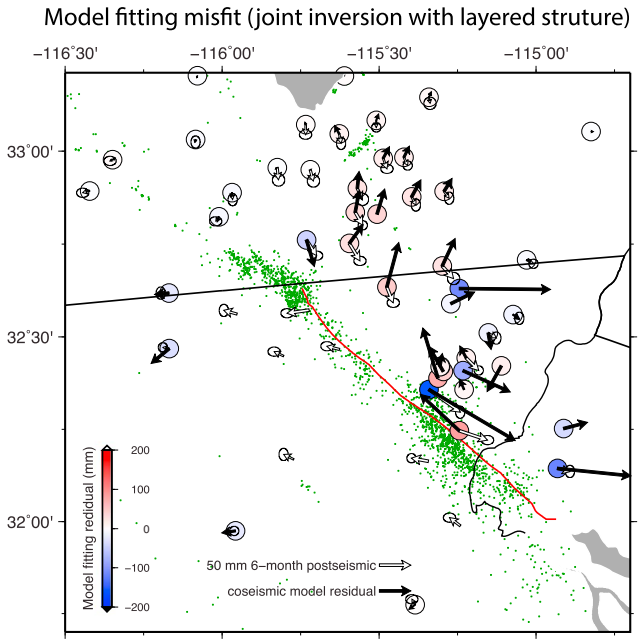

Figure 6. Model fitting residuals (black arrows) and the first 6 month postseismic displacement (white arrows; data from *Gonzalez-Ortega et al*. [2014]). The colors in the circles represent the model underfitting (blue) or overfitting (red).

produce more slip at greater depth [*Hearn and Bürgmann*, 2005], which is shown in Figures 4 and 5b. As a result, the choice of Earth structure may not change the predicted surface displacements, but it could affect the fault slip distribution significantly.

The moment estimated from the layered Earth structure is ~20% higher than from the homogeneous structure (Table 3) due to more deep slip and a higher shear modulus at 10–15 km depth. The moment magnitude of the inferred slip model is M_w 7.28 and is close to the geodetic inversion by *Wei et al*. [2011], seismic inversions by *Hauksson et al*. [2011] and *Melgar et al*. [2012], and the seismic and geodetic combined study by *Wei et al*. [2011]. The amount of deep slip is especially important for calculating postseismic deformation from afterslip and viscous relaxation at depth, because it changes the magnitude of coseismic stress changes in the lower crust and upper mantle.

5.4. Model Fitting Residuals

In the joint inversion there seems to be a systematic bias in the model fitting residuals (black arrows in Figure 6). In order to determine if this systematic pattern in the residuals relates to early postseismic displacement included in our InSAR data, we compare fitting residuals from the joint inversion with early postseismic GPS and InSAR measurements from *Gonzalez-Ortega et al*. [2014]. Figures 6 and 7 show the joint inversion-based model fitting residuals of GPS and InSAR data sets, respectively. In Figure 6, the black and white arrows are the model fitting residual (data-model prediction) and the first 6 month postseismic GPS measurements, respectively. The colored circles show if the fitting residual is overfitting (red) or underfitting (blue) the coseismic GPS measurements. The transition from blue to red from west to east sides of the fault surface rupture indicates a systematic bias of fitting residual. On the other hand, if we compare the azimuth and sign of residuals (black arrows in Figure 6), we find that most of the underfitting residuals are westward or southwestward, whereas overfitting residuals are northward or northeastward. This pattern of movement is similar to some of the postseismic GPS measurements (white arrows in Figure 6), especially stations west of the surface ruptures. For stations east of the surface rupture, however, most of the fitting residuals are southward, whereas postseismic movement is northward. As a result, there is not a clear indication that the model fitting residual of GPS data can be explained by early postseismic displacement. The systematic underfitting and overfitting patterns could possibly imply a lateral heterogeneity of elastic structure between the Peninsular Ranges and the Salton Trough due to different crustal thickness and material properties shown in tomographic studies [e.g., *Tape et al*., 2009, 2012; *Shaw et al*., 2015].

For the InSAR fitting residual, there seems to be systematic residuals east or west of the surface ruptures in both InSAR-only and joint inversions (Figures 7a, 7b, and S1). Figures 7c and 7d represent the early (4 or 5 months) postseismic displacement based on Envisat SAR acquisitions. For the fitting residual of ascending InSAR (Figure 7a), there is a systematic overfitting (red) northeast of the surface ruptures and underfitting residual south and southeast of the ruptures. For the descending InSAR (Figure 7b), there is overfitting around the north portion of the fault, whereas generally underfitting around south portion of the fault. The underfitting in the southern part of the fault is in agreement with early postseismic subsidence (blue area in Figures 7c and 7d) due to postseismic afterslip [*Gonzalez-Ortega et al*., 2014]. The overfitting residual

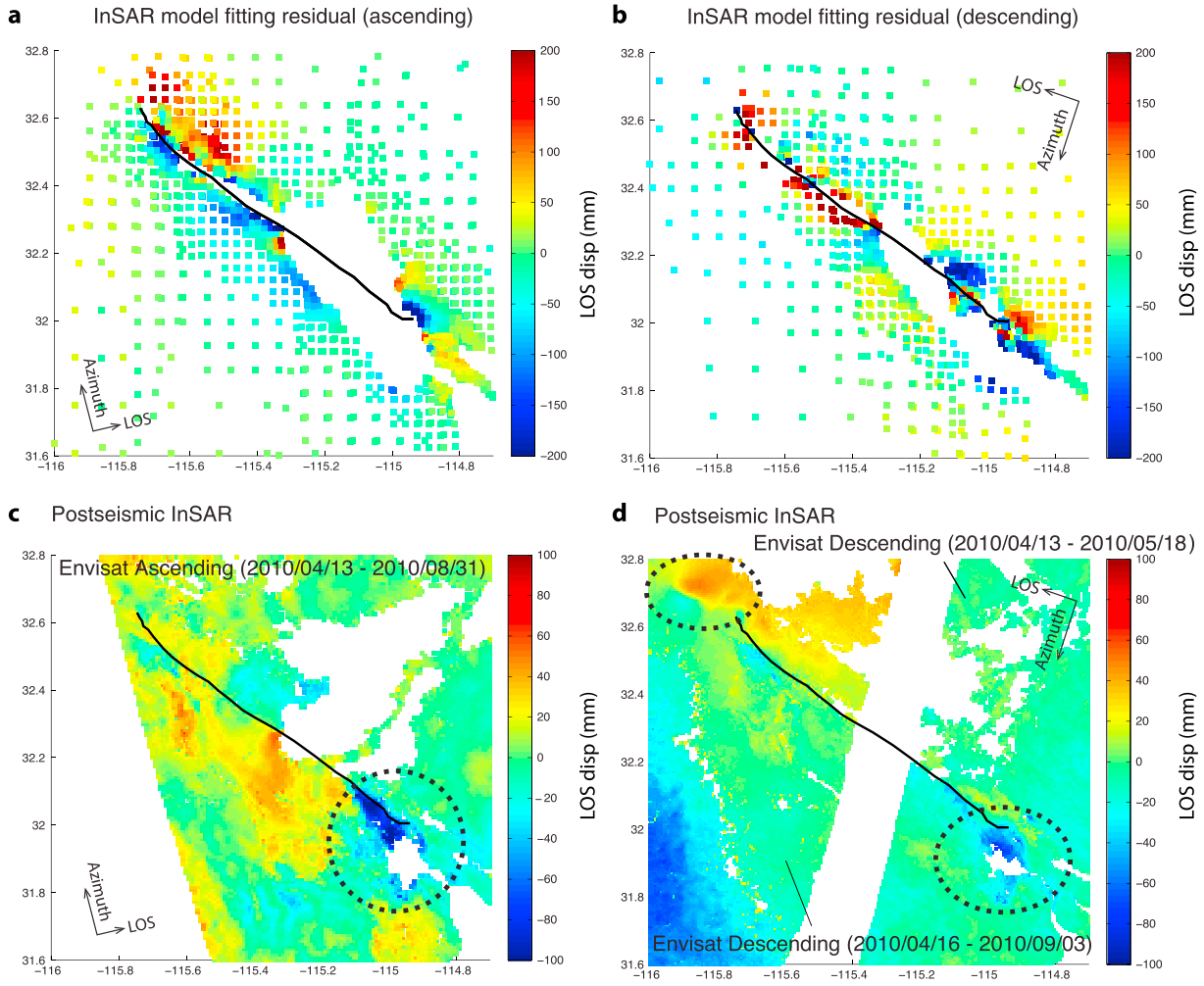

Figure 7. (a) Model fitting residual of ascending InSAR pairs. (b) Model fitting residual of descending InSAR pairs. (c) Early ascending postseismic interferogram (track A306). (d) Early descending postseismic interferograms (tracks D356 and D313). Here positive (warm color) is toward the satellite. The dashed circles in Figures 7c and 7d highlight the postseismic displacement.

northeast of the northern part of the fault seems to correlate with postseismic uplift shown in red in Figure 7d. The rest of the fitting residuals may relate to oversimplified fault geometry in the near-field and atmospheric noise (e.g., tropospheric water vapor and ionospheric variations) in InSAR. It is not easy to see systematic underfitting or overfitting residuals to the west or east of the surface ruptures from InSAR, but part of the small-scale misfit can be explained by early postseismic displacement. Incorporating GPS measurement near the EMC ruptures may help to elucidate the effect of the lateral heterogeneous contribution to coseismic displacement for the EMC event.

5.5. Fault Complexity and Shallow Slip Deficit

Based on the synthetic checkerboard test (Figure S4), the shallower patches have better constrained slip than the deeper patches. The slip standard deviation (Figure 6a) also implies more consistency of shallow slip using multiple data constraints. In the deeper part of the fault, the higher standard deviation in slip and poorer model resolution are likely due to the filtering effect of elastic deformation within a medium, more limited far-field geodetic data coverage (e.g., GPS); lower displacement amplitude with relatively higher data uncertainty (e.g., subpixel offset); and the oversimplified layered Earth structure (Table S1) used in this study. Nevertheless, despite higher standard deviations in slip revealing the uncertainty of deep slip, the calculated M_w for layered inversions using different data constraints (Table 3) are quite consistent (M_w 7.20–7.32).

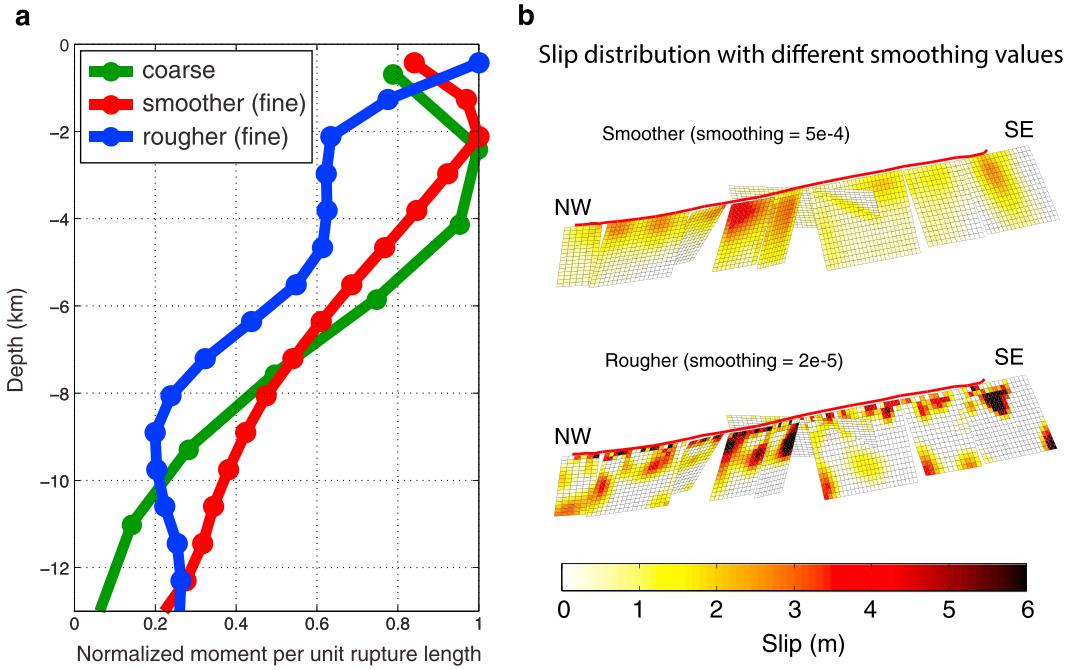

Figure 8. (a) Comparison of slip distribution with depth for the EMC event. Note that the subfault size is 2 km × 2 km for the coarse model and 1 km × 1 km for the fine model. The green line is the slip profile with coarse slip model, and the blue and red lines are the slip profiles with lower (rougher) and higher (smoother) smoothing values, respectively. (b) Perspective views of the slip distribution from inversions with (top) higher and (bottom) lower smoothing values.

Our preferred result (Figure 6c) shows dip angle variation along strike and more distinct slip patches that are surrounded by aftershocks. The complexity of the EMC surface ruptures in the Sierra Cucapah "sierra domain" [e.g., *Hauksson et al*., 2011; *Oskin et al*., 2012; *Fletcher et al*., 2014] involving multiple fault strands (e.g., in Yuha desert, north of the Sierra Cucapah [*Kroll et al*., 2013]) implies that a relatively simple fault geometry like the one proposed in this study may not be sufficient to explain the detail of fault slip on individual subfault strands near the surface. Additionally, other physical processes during the earthquake, such as liquefaction and inelastic deformation, influence the inferred slip at shallow depths. However, our fault geometry and slip distribution are sufficient to explain the coseismic geodetic data used here.

Fialko et al. [2005] described a systematic reduction of slip at the shallowest fault depths (shallower than 2 km) that they called the "shallow slip deficit (SSD)." This observation was based on geodetic inversions from the M_w 7.3 Landers, the M_w 7.0 Hector Mine, the M_w 7.6 Izmit, and the M_w 6.5 Bam earthquakes. They suggest that the origin of the SSD is that the uppermost crust around young and developing faults undergoes inelastic deformation in the interseismic period because the top 2–3 km of the crust is not able to accumulate significant elastic strain. They conclude that the coseismic slip on the shallowest part of the fault is less than slip below this depth because the preearthquake stress is lower.

In this study, which considers both near-field (InSAR and subpixel offsets) and far-field (mostly GPS) geodetic constraints, we calculate average slip over the whole length of the fault at different fault depths (Figure 8a). We also find a reduced slip at the shallowest (0–1 km) depth based on the joint inversion with the fault geometry composed of 552 2 km × 2 km subfault patches (the green curve in Figure 8a). The average slip at the shallowest depth is ~80% of the peak slip at 3 km depth in the joint inversion. As an experiment, we decrease the subfault patch size to 1 km × 1 km in a fault geometry composed of 2208 patches (Figure 8b). We keep the same data weighting and vary smoothing value in order to test if there is a trade-off between model roughness and SSD. Our result suggests higher shallow slip deficit (SSD) when the slip model is smoother (red line in Figure 8a), whereas no SSD when the slip is rougher (Figure 8b). With finer fault patch size and lower smoothing, the peak-inferred slip is at the shallowest depth and the slip gradually decreases with depth. In other words, there is no shallow slip deficit for the EMC earthquake in the northern part of the rupture for the result with finer fault patch size. This result suggests that when near-field measurements are

available and the subfault patch size is sufficiently small, we can reduce the SSD by tuning the smoothing parameter. However, the shallowest slip of the "rougher" model (Figure 8b) shows highly heterogeneous slip distribution. This distribution could be due to oversimplified shallow Earth structure and fault geometry, inelastic deformation at the shallowest depth, or the shallow fault slip occurred on several nearby fault segments instead of a single fault plane along strike [e.g., *Fletcher et al*., 2014]. Without including all of these shallow complexities in the model, the joint inversion would try to explain all of the near-field measurements by contributing a heterogeneous slip distribution when the smoothing parameter is lower. A recent study by *Xu et al*. [2016] also finds a reduction of SSD for the Landers, Hector Mine, and EMC events based on improved near-field InSAR and subpixel offset data.

On the other hand, the coseismic surface displacements in the Bam earthquake are continuously distributed within a 500 m to 1 km wide fault zone [*Fialko et al*., 2005; *Fielding et al*., 2005, 2009], which implies reduced fault slip at the shallowest depth or distributed shear in the uppermost crustal layers. The postseismic deformation after the Bam earthquake revealed an unusual pattern of subsidence that could be due to dilatancy recovery in the shallow shear zone [*Fielding et al*., 2009]. Besides, for the Bam earthquake, the maximum surface displacement measured in the field is ~10% of coseismic peak slip at depth [e.g., *Funning et al*., 2005], whereas it is more than 50% for the Landers, Hector Mine, or EMC earthquakes [e.g., *Simons et al*., 2002; *Kaverina et al*., 2002; *Xu et al*., 2016; *Milliner et al*., 2015; this study]. These observations and slip models imply a fundamental difference of near-fault coseismic displacement between the Bam earthquake and the other events mentioned above. To conclude, we find that inversions with finer fault patch size and geometry as well as near-field geodetic measurements can properly recover coseismic slip at the shallowest depth. The magnitude of the SSD may thus not apply globally and perhaps varies depending on local upper crustal fault zone properties.

6. Conclusions

In this study, we invert for coseismic slip of the 2010 M_w 7.2 El Mayor-Cucapah earthquake using GPS, InSAR, and subpixel offset data sets. Our optimized fault geometry indicates that the five fault planes north of the epicenter are NE dipping, whereas three fault segments south of the epicenter are SW dipping. The dips are well constrained by the pixel offsets. The model also includes an east dipping normal fault that initiated the earthquake. The inferred slip is relatively shallow and mostly distributed between 0 and 10 km depth along the ~120 km NW-SE fault trace. The slip distribution based on the joint inversion shows that the peak slip is near the center of the fault system where the epicenter is located, and another higher slip patch is resolved at the southern end of the fault geometry. Synthetic checkerboard tests indicate that the spatial resolution of coseismic slip is dependent on data constraints. Given geodetic data spatial sampling and the uncertainty of each data set, the slip model has higher resolution at shallower depth and fails to resolve distinct slip patches at the bottom of the model fault planes. We find that considering different Earth structures results in a 60% difference in the amount of inferred deep slip. Including near-field geodetic data such as InSAR and subpixel offset of SAR images, and finer subfault patch size, we find peak slip at the shallowest depth (0–2 km) for the EMC event that contradicts the proposed shallow slip deficit found for the 2003 Bam earthquake and some previous EMC studies. This result implies that peak slip depth can be influenced by the choice of data constraints and fault model discretization and smoothing, which is independent of fault zone properties and tectonic loading, in addition to true variations in fault slip.

Acknowledgments

We highly appreciate the careful review and the comments by Associate Editor E. Hill, G. Funning, and an anonymous reviewer, which significantly improved the quality of this manuscript. Original Envisat SAR data are copyright ESA and were provided under ESA data grant AOE-668 and data licenses to UNAVCO for the EarthScope and WInSAR projects. Original ALOS SAR data are copyright JAXA and were provided through the Alaska Satellite Facility. The PBO GPS data are available at the UNAVCO website (ftp://data-out.unavco.org/pub/products/sinex/). The SCEC community velocity model is available at the website (http://scec.usc.edu/scecpedia/Community_Velocity_Model). The first-year aftershock catalog is from CICESE (http://resnom.cicese.mx/). The joint inversion based slip distribution can be found in Table S1. We thank D. Dreger for providing the codes for computing data weighting, smoothing, and geodetic inversions. S. Leprince provided the digital versions of his COSI-Corr analysis of SPOT images. We would like to thank CICESE for the GPS installation and acquisition and X. Xu for sharing their shallow slip deficit results. Part of this research was supported by the NASA Earth Surface and Interior Focus Area and performed at the Jet Propulsion Laboratory, California Institute of Technology. M.-H. Huang is supported by an appointment to the NASA Postdoctoral Program at the Jet Propulsion Laboratory, administered by Oak Ridge Associated Universities through a contract with NASA.

References

Blackwell, D., and M. Richards (2004), Geothermal map of North America: American Association of Petroleum Geologists scale 1:6,500,000, Tulsa, Okla.

Bürgmann, R., P. A. Rosen, and E. J. Fielding (2000), Synthetic aperture radar interferometry to measure Earth's surface topography and its deformation, *Annu. Rev. Earth Planet. Sci.*, *28*, 169–209.

Cattin, R., P. Briole, H. Lyon-Caen, P. Bernard, and P. Pinettes (1999), Effects of superficial layers on coseismic displacements for a dip-slip fault and geophysical implications, *Geophys. J. Int.*, *137*, 149–158.

Chen, C. W., and H. A. Zebker (2002), Phase unwrapping for large SAR interferograms: Statistical segmentation and generalized network models, *IEEE Trans. Geosci. Remote Sens.*, *40*(8), 1709–1719.

Du, Y., P. Segall, and H. Gao (1997), Quasi-static dislocations in three dimensional inhomogeneous media, *Geophys. Res. Lett.*, *24*, 2347–2350, doi:10.1029/97GL02341.

Fialko, Y., D. Sandwell, M. Simon, and R. Rosen (2005), Three-dimensional deformation caused by the Bam, Iran, earthquake and the origin of shallow slip deficit, *Nature*, *435*, 295–299.

Fielding, E. J., M. Talebian, P. A. Rosen, H. Nazari, J. A. Jackson, M. Ghorashi, and R. Walker (2005), Surface ruptures and building damage of the 2003 Bam, Iran, earthquake mapped by satellite synthetic aperture radar interferometric correlation, *J. Geophys. Res.*, *110*, B03302, doi:10.1029/2004JB003299.

Fielding, E. J., P. R. Lundgren, R. Bürgmann, and G. J. Funning (2009), Shallow fault-zone dilatancy recovery after the 2003 Bam earthquake in Iran, *Nature*, *458*, 64–68, doi:10.1038/nature07817.

Fletcher, J. M., et al. (2014), Assembly of a large earthquake from a complex fault system: Surface rupture kinematics of the 4 April 2010 El Mayor-Cucapah (Mexico) M_w 7.2 earthquake, *Geosphere*, *10*, 797–827, doi:10.1130/GES00933.1.

Funning, G. J., B. Parsons, T. J. Wright, J. A. Jackson, and E. J. Fielding (2005), Surface displacements and source parameters of the 2003 Bam (Iran) earthquake from Envisat advanced synthetic aperture radar imagery, *J. Geophys. Res.*, *110*, B09406, doi:10.1029/2004JB003338.

Gold, P. O., M. E. Oskin, A. J. Elliott, A. Hinojosa-Corona, M. H. Taylor, O. Kreylos, and E. Cowgill (2013), Coseismic slip variation assessed from terrestrial lidar scans of the El Mayor-Cucapah surface rupture, *Earth Planet. Sci. Lett.*, *366*, 151–162, doi:10.1016/j.epsl.2013.01.040.

Gonzalez-Ortega, A., Y. Fialko, D. Sandwell, F. A. Nava-Pichardo, J. Fletcher, J. Gonzalez-Garcia, B. Lipovsky, M. Floyd, and G. Funning (2014), El Mayor-Cucapah (M_w 7.2) earthquake: Early near-field postseismic deformation from InSAR and PGS observations, *J. Geophys. Res. Solid Earth*, *119*, 1482–1497, doi:10.1002/2013JB010193.

Hauksson, E., J. Stock, K. Hutton, W. Yang, J. A. Vidal-Villegas, and H. Kanamori (2011), The 2010 M_w 7.2 El Mayor-Cucapah Earth sequence, Baja California, Mexico and southernmost California, USA: Active seismotectonics along the Mexican Pacific margin, *Pure Appl. Geophys.*, *168*, 1255–1277, doi:10.1007/s00024-010-0209-7.

Hearn, E. H., and R. Bürgmann (2005), The effect of elastic layering on inversions of GPS data for earthquake slip and stress changes, *Bull. Seismol. Soc. Am.*, *95*, 1637–1653.

Herring, T., R. King, and S. McClusky (2008), Introduction to GAMIT/GLOBK report, Mass. Inst. of Technol., Cambridge.

Huang, M.-H., D. Dreger, R. Bürgmann, S.-H. Yoo, and M. Hashimoto (2013), Joint inversion of seismic and geodetic data for the source of the 2010 March 4, M_w 6.3 Jia-Shian, SW Taiwan, earthquake, *Geophys. J. Int.*, *193*, 1608–1626.

Ingber, L. (1993), Simulated annealing: Practice versus theory, *J. Math. Comput. Modell.*, *18*, 29–57.

Kaverina, A., D. Dreger, and E. Price (2002), The combined inversion of seismic and geodetic data for the source process of the 16 October 1999 M_w 7.1 Hector Mine, California, earthquake, *Bull. Seismol. Soc. Am.*, *92*, 1266–1280.

Kroll, K. A., E. S. Cochran, K. B. Richards-Dinger, and D. F. Sumy (2013), Aftershocks of the 2010 M_w 7.2 El Mayor-Cucapah earthquake reveal complex faulting in the Yuha Desert, California, *J. Geophys. Res. Solid Earth*, *118*, 6146–6164, doi:10.1002/2013JB010529.

Lekic, V., S. W. French, and K. M. Fischer (2011), Lithospheric thinning beneath rifted regions of Southern California, *Science*, *334*, 783–787, doi:10.1126/science.1208898.

Leprince, S., S. Barbot, F. Ayoub, and J. P. Avouac (2007), Automatic and precise orthorectification, coregistration, and subpixel correlation of satellite images, application to ground deformation measurements, *IEEE Trans. Geosci. Remote Sens.*, *45*(6), 1529–1558, doi:10.1109/tgrs.2006.888937.

Lohman, R. B., and M. Simons (2005), Some thoughts on the use of InSAR data to constrain models of surface deformation: Noise structure and data downsampling, *Geochem. Geophys. Geosyst.*, *6*, Q01007, doi:10.1029/2004GC000841.

Melgar, D., Y. Bock, and B. W. Crowell (2012), Real-time centroid moment tensor determination for large earthquake from local and regional displacement records, *Geophys. J. Int.*, *188*, 703–718, doi:10.1111/j.1365-246X.2011.05297.x.

Michel, R., J.-P. Avouac, and J. Taboury (1999), Measuring ground displacements from SAR amplitude images: Application to the Landers earthquake, *Geophys. Res. Lett.*, *26*, 875–878, doi:10.1029/1999GL900138.

Milliner, C. W. D., J. F. Dolan, J. Hollingsworth, S. Leprince, F. Ayoub, and C. G. Sammis (2015), Quantifying near-field and off-fault deformation patterns of the 1992 M_w 7.3 Landers earthquake, *Geochem. Geophys. Geosyst.*, *16*, 1577–1598, doi:10.1002/2014GC005693.

Okada, Y. (1992), Internal deformation due to shear and tensile faults in a half space, *Bull. Seismol. Soc. Am.*, *82*, 1018–1040.

Oskin, M. E., et al. (2012), Near-field deformation from the El Mayor-Cucapah earthquake revealed by differential lidar, *Science*, *335*, 702–705, doi:10.1126/science.1213778.

Rosen, P. A., S. Hensley, and G. Peltzer (2004), Updated repeat orbit interferometry package released, *Eos Trans. AGU*, *85*(5), 47, doi:10.1029/2004EO050004.

Segall, P. (2010), *Earthquake and Volcano Deformation*, 432 pp., Princeton Univ. Press, Princeton, N. J.

Shaw, J. H., et al. (2015), Unified structural representation of the Southern California crust and upper mantle, *Earth Planet. Sci. Lett.*, *415*, 1–15, doi:10.1016/j.epsl.2015.01.016.

Simons, M., Y. Fialko, and L. Rivera (2002), Coseismic deformation from the 1999 M_w 7.1 Hector Mine, California, earthquake as inferred from InSAR and GPS observations, *Bull. Seismol. Soc. Am.*, *92*, 1390–1402.

Spinler, J., R. A. Bennett, C. Walls, S. Lawrence, and J. J. González García (2015), Assessing long-term postseismic deformation following the *M* 7.2 April 4, 2010 El Mayor-Cucapah earthquake with implications for lithospheric rheology in the Salton Trough, *J. Geophys. Res. Solid Earth*, *120*, 3664–3679, doi:10.1002/2014JB011613.

Sun, J., Z.-K. Shen, R. Bürgmann, M. Wang, L. Chen, and X. Xu (2013), A three-step maximum a posteriori probability method for InSAR data inversion of coseismic rupture with application to the 14 April 2010 M_w 6.9 Yushu, China, earthquake, *J. Geophys. Res. Solid Earth*, *118*, 4599–4627, doi:10.1002/jgrb.50244.

Tape, C., Q. Liu, A. Maggi, and J. Tromp (2009), Adjoint tomography of the Southern California crust, *Science*, *325*, 988–992, doi:10.1126/science.1175298.

Tape, C., A. Plesch, J. H. Shaw, and H. Gilbert (2012), Estimating a continuous Moho surface for the California unified velocity model, *Seismol. Res. Lett.*, *83*, 728–735, doi:10.1785/0220110118.

Toda, S., R. S. Stein, V. Sevilgen, and J. Lin (2011), Coulomb 3.3 graphic-rich deformation and stress-change software for earthquake, tectonic, and volcano research and teaching—User guide, U.S. Geol. Surv. Open File Rep. 2011-1060, 63. [Available at http://pubs.usgs.gov/of/2011/1060/.]

Wang, R., F. Lorenzo Martín, and F. Roth (2003), Computation of deformation induced by earthquakes in a multi-layered elastic crust: FORTRAN programs EDGRN/EDCMP, *Comput. Geosci.*, *29*, 195–207.

Wei, S., et al. (2011), Superficial simplicity of the 2010 El Mayor-Cucapah earthquake of Baja California in Mexico, *Nat. Geosci.*, *4*, 615–618.

Xu, X., X. Tong, D. T. Sandwell, C. W. D. Milliner, J. F. Dolan, J. Hollingsworth, S. Leprince, and F. Ayoub (2016), Refining the shallow slip deficit, *Geophys. J. Int.*, *204*, 1867–1886.